SPE 144050

Submicron-Pore Characterization of Shale Gas Plays

Malek Elgmati; Hao Zhang; Baojun Bai; Ralph Flori, SPE, Missouri University of Science & Technology and Qi Qu, SPE, Baker-Hughes Company

Abstract

Gas storage and flow behavior in the shale gas rocks are complex and hard to identify by conventional core analysis. This study integrates clustering analysis techniques from material science, petrophysics, and petrology to characterize North American shale gas samples from Utica, Haynesville, and Fayetteville shale gas plays. High pressure (up to 60,000 psi) mercury porosimetry analysis (MICP) determined the pore size distributions. A robust, detailed tomography procedure using a dual-beam (Scanning Electron Microscope and Focused Ion Beam, also called SEM-FIB) instrument successfully characterized the submicron-pore structures. SEM images revealed various types of porosities. Pores on a scale of nanometers were found in organic matter; they occupy 40−50% of the kerogen body. Two-hundred two-dimensional SEM images were collected and stacked to reconstruct the original pore structure in a three-dimensional model. The model provided insights into the petrophysical properties of shale gas, including pore size distribution, porosity, tortuosity, and anisotropy. This paper presents the pore model constructed from Fayetteville shale sample. The work used X-ray diffraction (XRD) to semi-quantify shale gas clay and non-clay minerals. The Haynesville and Utica (Indian Castle formation) shale samples have a high illite content. The Utica (Dolgeville formation) shale samples show high calcium carbonate (calcite) content. Moreover, wettability tests were performed on the shale samples, and the effect of various fracturing fluid additives on their wettability was tested. Most additives made the shale gas surfaces hydrophilic-like (water-wet).

Introduction

Unconventional natural gas resources have grown in importance as a complement to conventional fossil fuels as world energy demand has increased. Shale gas is the second largest unconventional energy resource after heavy oil. Recently, the United States Geological Survey (USGS) estimated that tight sands and gas shale in the United States may hold up to 460 Tcf of gas. There are about 200,000 unconventional gas wells in low-permeability sands, coal-bed methane deposits, and shale gas in the lower 48 states. Shale gas is more environmentally friendly and attractive compared to other energy resources due to its ecological advantages (low levels of carbon dioxide CO_2 emission) and safety qualities (insignificant sulfur dioxide contents, H_2S%).

Many petrophysical properties of the unconventional tight gas formations are significantly different from those of conventional reservoirs. In particular, such formations have nano-scale pores and channels, a unique pore structure, and the unusual wettability, transport, and storage properties. These differences produce the fluid flow mechanisms different from those in conventional gas plays, especially when the size of the pore throats differs from the size of the saturating fluid molecules by only slightly more than one order of magnitude. Despite the practical importance of this topic, very little is known about it.

Commercial production from extremely low permeability gas reservoirs requires hydraulic fracturing stimulation at the beginning of well production. Proper selection of a fracturing fluid is key to successful stimulation. Currently, selection of hydraulic fracturing fluids for unconventional gas wells borrows from conventional oil and gas techniques. However, shale gas plays have unique properties. For example, the size of the pore throats in shale may differ from the size of the saturating fluid molecules by only slightly more than one order of magnitude. The physics of the fluid flow in these rocks, with permeabilities in the nanodarcy range, is poorly understood.

Key to successful characterization of fluid flow behavior in shale gas plays is an understanding of the petrophysics of shale rocks and their submicron pore structures. A few studies have attempted to construct submicron pore structures. Liviu et al. (2007) conducted an intensive study of submicron pore imaging using SEM-FIB for chalk rocks. Sondergeld et al. (2010) used the same method to characterize the submicron structures of a few shale gas plays. However, no attempt has yet been made to systematically characterize the petrophysical properties of shale gas plays with any means other than submicron pore imaging.

This work used high pressure mercury porosimetry analysis, or MICP (up to 60,000 psi) to determine pore throat distribution and pore volume. It used a dual-beam system (SEM/FIB) to reconstruct three-dimensional structural pore models of shale gas samples. Energy-dispersive spectroscopy (EDS) confirmed the existence of organic matter (kerogen) and defined the elemental composition of the examined shale gas samples. A modest clay mineralogy study was conducted by using X-ray diffractometer. Contact angle measurements evaluated surface wetting properties.

Mercury Porosimetry (MICP)

Mercury (Hg) is a toxic material that has been used in rock laboratories as an indirect measure of rock capillarity and porosimetry. These experiments are considered destructive, expensive, and time consuming. Nevertheless, mercury porosimetry has been widely accepted as a mean to characterize porous solids with respect to their pore volume (porosity) and pore size distribution over a wide range of pore sizes. Mercury is nonwetting phase and it can only access interconnected pores. The volume of mercury that can enter pore spaces is limited by the maximum pressure attained during analysis. MICP has produced representative and reproducible results for conventional reservoir rocks. However, for shale gas rocks, the scenario is almost impossible to reproduce due to the shale tightness. Only two of 12 attempts have been successful, although high injection pressures up to 60,000 psi were applied. This pressure level is still greater by a factor of 5 than that determined by curve of water drainage displaced by air.

The mercury capillary pressure curves are dependent upon (1) pore size distribution and tightness, (2) rock and fluid type, and (3) saturation history (intrusion and extrusion processes). Data extracted from saturation and desaturation curves always show differences in pore size distribution. Extrusion data often indicate smaller pores than intrusion data. This discrepancy is attributable to intrusion and extrusion hysteresis, which is dependent on the saturation process (Leverett, 1941). It is also likely due to alterations in the advancing and receding mercury contact angles, and to mercury entrapment. Mercury porosimetry is traditionally calculated as:

$$p = \frac{-2\sigma \cos\theta}{r} \qquad (1)$$

where, p is the pressure that must be applied to nonwetting liquid (mercury) to penetrate cylindrical pores of radius r, and σ and θ are the mercury surface tension and contact angle, respectively. This equation indicates that, as pressure increases, the mercury intrudes into progressively narrower pores as long as the surface tension and contact angles remain constant.

This work used small volumes and weights (1−3 grams), despite claims by some researchers that this approach can minimize the credibility of capillary pressure values. However, studies by Wardlaw and Taylor (1976), Ghosh et al. (1987), and Kopaska-Merkel and Amthor (1988) have shown that small sample weight has no significant effect on mercury porosimetry.

This project carried out two successful MICP experiments using Utica and Haynesville shale samples. **Fig. 1** presents mercury intrusion and extrusion curves of Utica shale alongside the resulting pore size histogram. It shows possible tiny fractures that exhibit little instant intrusion due to the raise of mercury head in the penetrometer. After an incremental pressure was applied, mercury began intruding into open connected pores. Effective porosity can only be quantified using this method. Once pressure reached the upper limit, the extrusion process began, while pressure decreased incrementally to atmospheric pressure (~14.7 psi). Both pressure and cumulative intruded and extruded mercury volumes were monitored. The crooked curve of the intrusion and extrusion process is an indicator of various pore sizes and/or different flow units. Pore throat diameter can be calculated using **Eq. 1** and a known mercury surface tension of 480 dynes/cm and contact angle of 140° for mercury. **Fig. 1** shows a statistical pore size distribution based on intruded mercury volume data. The resulting Utica shale median pore throat diameter was 30 nm. Most of the intruded mercury occurred between 3,500 and 21,000 psi, a level corresponding to a pore throat diameter of 10−60 nm and certainly a result of shale pore structure and mineral texture. Residual mercury saturation was 23.3%. Sondergeld et al. (2010) reported that MICP porosimetry underestimates the pore radii more than SEM imaging results. Because this method is destructive and sponsors can provide only limited quantities of shale gas rock, this work did not include the comparison study originally proposed. However, future studies should demonstrate the correlation between MICP and three-dimensional SEM pore histogram results.

Numerous attempts have been made to relate the permeability of a solid to intrinsic and more readily measurable properties, such as porosity and pore diameter. Kozeny models the flow of fluids across straight cylindrical channels in a bed of rock by combining Darcy's and Poiseuille's laws to obtain

$$k = \frac{\phi \, d_p^2}{32 \, \tau} \qquad (2)$$

where ϕ is the rock porosity, d_p is the average (mean volume) diameter of the pores, and τ is the tortuosity coefficient. This equation assumes the tortuosity coefficient is equal to 1 (i.e., the pores are assumed to be straight, cylindrical capillaries).

Using the Kozeny simplified formula, the permeability of Utica shale sample was estimated to 4.15×10^{-3} md, with a porosity of 14.56%.
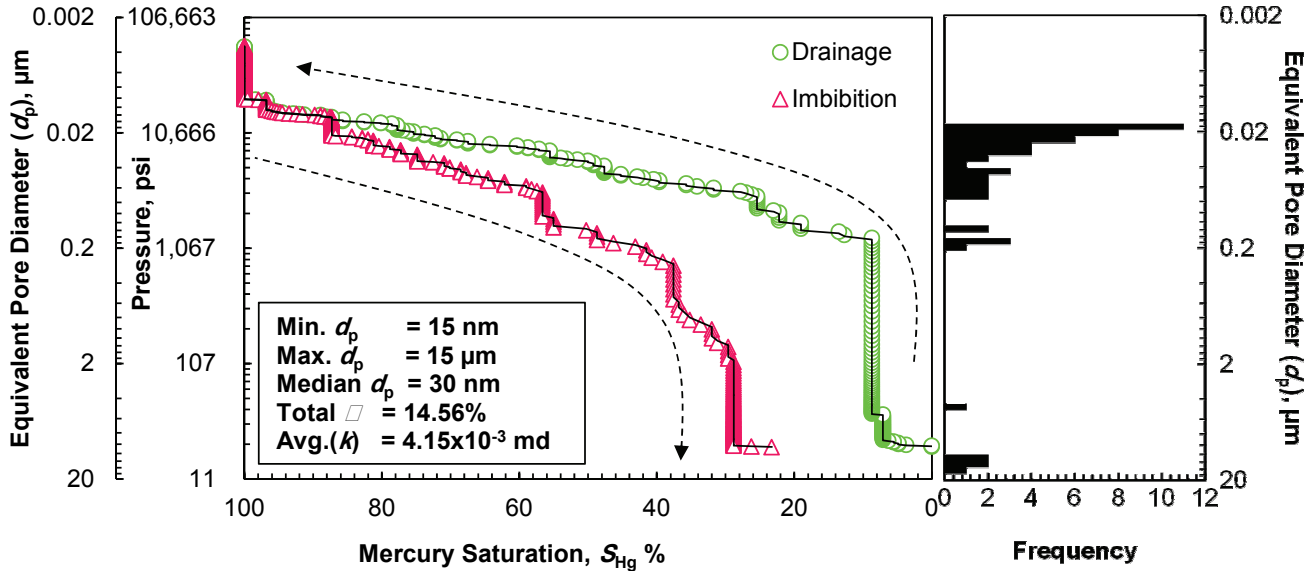

Fig. 1−Mercury intrusion and extrusion data and pore size distribution of intrusion data for Utica shale, Dolgeville Fm., at a depth of 5,197 ft.

Fig. 2 presents another successful MICP test for the Haynesville shale sample. It suggests that about 35% of the mercury was initially intruded before any pressure was applied. It also shows a possible fracture 15 µm wide. This crack could tremendously increase gas deliverability and storability. The computed permeability represents the majority of nano pore networks. Most mercury intrusion occurred between 10,600 and 60,000 psi, which is equivalent to a pore throat diameter of 4−20 nm. The Haynesville shale has extremely low permeability of 1.38×10^{-4} md, mainly because of the nano pore level, which is peculiar to shale gas. The total entrapped mercury is 61.3%, which includes the remaining mercury in the possible open crack. Thus, the net residual mercury in the nano pores would be 26.66%.
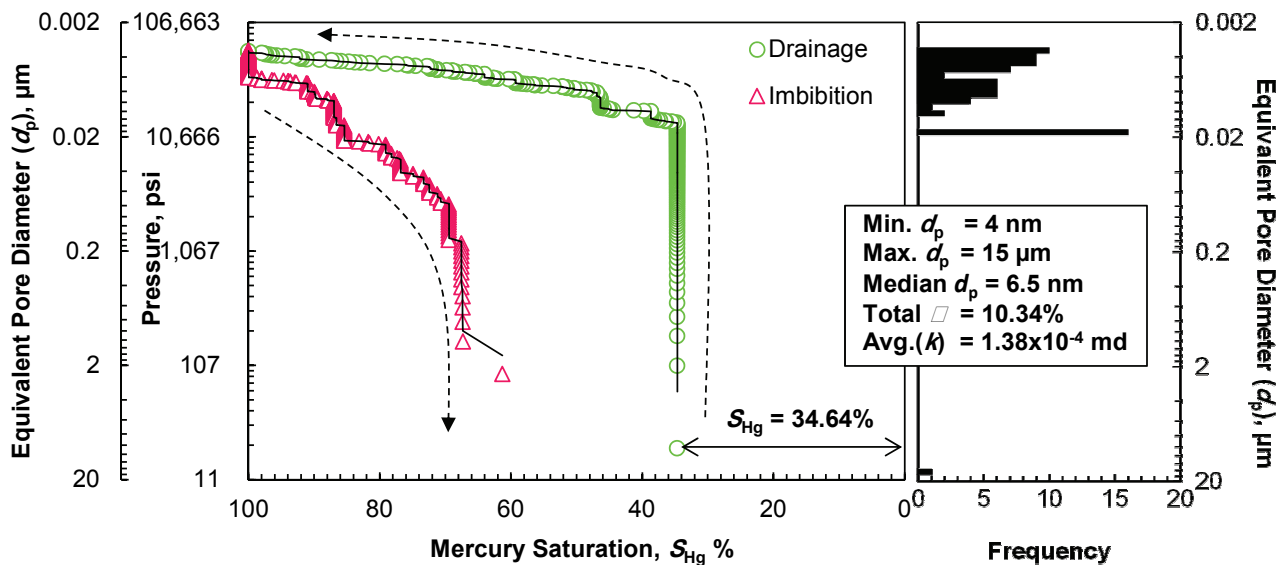

Fig. 2−Mercury intrusion and extrusion data and pore size distribution of intrusion data for Haynesville shale at a depth of 12,000 ft.

SEM Imaging and FIB Sequential Milling

The dual-beam system (SEM-FIB) has been widely used in material science studies. It is especially useful for three-dimensional microscopy and material characterization. Its electron gun offers in situ imaging, and the focused ion beam provides simultaneous sequential milling. Many electron detectors are associated with a dual-beam microscope. This work relied primarily on three detectors to detect the electrons and rays ejected from the targeted specimen when it was attacked by the electron beam. The ejected electrons included secondary electrons (SE) and backscattered electrons (BSE) for imaging. An energy dispersive spectroscope (EDS) detector permitted element mapping. A BSE detector is preferable for imaging because it minimizes surface electron charges. However, an SE detector can also produce satisfactory images. Shale gas rock, however, is nonconductive. Super electron charges are very likely to occur on the exposed surface. Therefore, this case demanded the use of a low voltage electron beam (2−5 kV) on the SEM side when a high electron beam current (0.17−1.4 nA) was used. This technique provides better image at high magnification. **Fig. 3** shows the standard dual-beam setup for shale gas serial sectioning and imaging. The stage must be tilted at 52° to make the ion beam normal to the specimen.
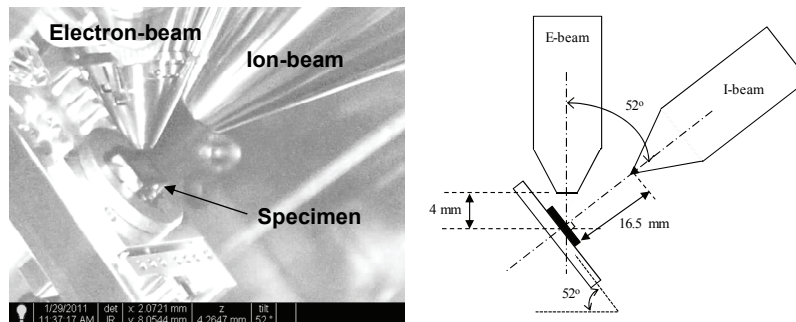

Fig. 3−Dual-beam microscope with loaded shale sample at 52° tilt.

Following is a detailed description of the optimum submicron pore imaging procedure used in this study.

(1) *Saw and polish small rock slices*. Specimens were prepared by sawing the rock into pieces measuring 5×5×2 mm. **Fig. 4** shows two common types of fractures, nonconductive and conductive, that have been observed in Utica shale while sawing; they are marked by A and B respectively. Conductive fractures may be drilling induced or natural, whereas nonconductive fractures are mostly healed by calcite. Macro conductive fractures are bridge-like, and they act along micro- or nano fractures to transport the adsorbed and free gas to the wellbore.
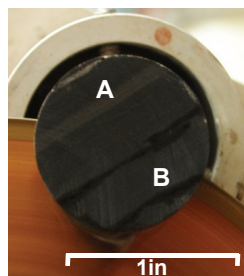

Fig. 4−Sawing a Utica shale sample from the Indian Castle Fm. at a depth of 4,649 ft: (A) Calcareous healed natural fractures, and (B) Either conductive natural fractures or drilling-induced cracks.

Specimens should be polished with the finest sand paper to give them a flat, smooth surface for better milling rate and time. Polishing was once believed to destroy the natural surface features; however, FIB mills beneath the surface to explore the undamaged clay structure. Fresh surfaces were usually used, although these require a longer milling time due to nonuniform milling surface.

(2) *Glue and coat sample plates*. The specimen was attached to an aluminum stub using carbon glue. Image drift is the most challenging problem in three-dimensional image stacking. Three types of drifts are possible: specimen drift, mechanical stage drift, and ion beam drift. Carbon glue can effectively attach the specimen to the stub, dramatically reducing specimen drift. To avoid mechanical stage drift during the FIB slicing procedure, the sample dimensions were kept as small as possible. Nonetheless, slight drift can occur as a result of an ion beam alignment disorder. A calibrated FIB with a highly focused ion beam alignment was used to eliminate this drift. Since shale rock is nonconductive material, a coating of gold and palladium is the most suitable material to increase sample conductivity and to lessen the electron charge on the surface. Moreover, this coating prevented interference with the carbon that exists naturally in the specimen within the organic matter.

(3) *Load prepared specimen into dual-beam instrument*. Once the specimen stub was pinned in the dual-beam stage and the chamber was vacuumed, the electron beam current and voltage were optimized for imaging. A flat surface spot was selected, and the stage was tilted 52° for milling. To protect the target area from damage, a layer of platinum measuring $10 \times 10 \times 1.5$ μm was deposited on the target area by sputtering; this process took approximately 18 minutes. A large volume of the rock material was removed from around the covered spot to ease the serial sectioning and imaging. This process consumed as much as one third of the total job time. The swimming pool was milled away and cleaned in two stages: First, a rough cut of a $25 \times 25 \times 20$ μm sample was made using regular cross-sectioning at the highest possible current (21 nA) in front of the targeted area, and silicon was applied. This step takes 20−35 minutes, depending on the milled volume and material. Two parallel pits measuring $7 \times 12 \times 20$ μm were then milled away using rectangular milling and a 9.3 nA current. This process takes another 30−40 minutes. Next, the surface exposed to the SEM gun was cleaned using a cleaning cross-section tool. Cleaning was performed in several steps, and the milling current was reduced to 93 pA for each step. This soft cut requires 30-60 minutes. The total preparation time ranges from 3 to 4 hours. Some samples suffered from serious curtains and redeposition of the milled material. To minimize redeposition, the swimming pool was deepened and widened. Ion beam curtaining is a vexing problem for image stacking. It highly relies on the milled material itself rather than the ion beam focus. Porosity, uneven phase, and platinum deposition are the major factors leading to curtaining in most situations. To diminish curtaining throughout the operation mode, low ion beam voltage (2−5 kV) was exploited. This method reduces curtains thickness to 2 nm. It can also be remedied by utilizing image smoothing algorithms associated with image programs.

(4) *Perform sequential FIB milling and SEM imaging*. Automated and sequential milling process removed $10 \times 0.05 \times 25$ μm (12.5 μm^3) rock material using 93 pA beam current and gold as an application. Exploiting gold in the milling application results in higher etching rate than using silica applications. After each milling step, a new two-dimensional surface image was captured by SEM. Each slice takes 4−5 minutes to mill and 30 minutes to obtain high resolution. This procedure was repeated 200 times. The total time required to mill $10 \times 10 \times 25$ μm rock sample was between 15 and 20 hours. The process can be speeded up by decreasing the objective milling volume or by increasing the milling beam current. Here, this task was accomplished using an automated program to ease the job. **Fig. 5** illustrates all the milling and cleaning steps and the serial sectioning process.
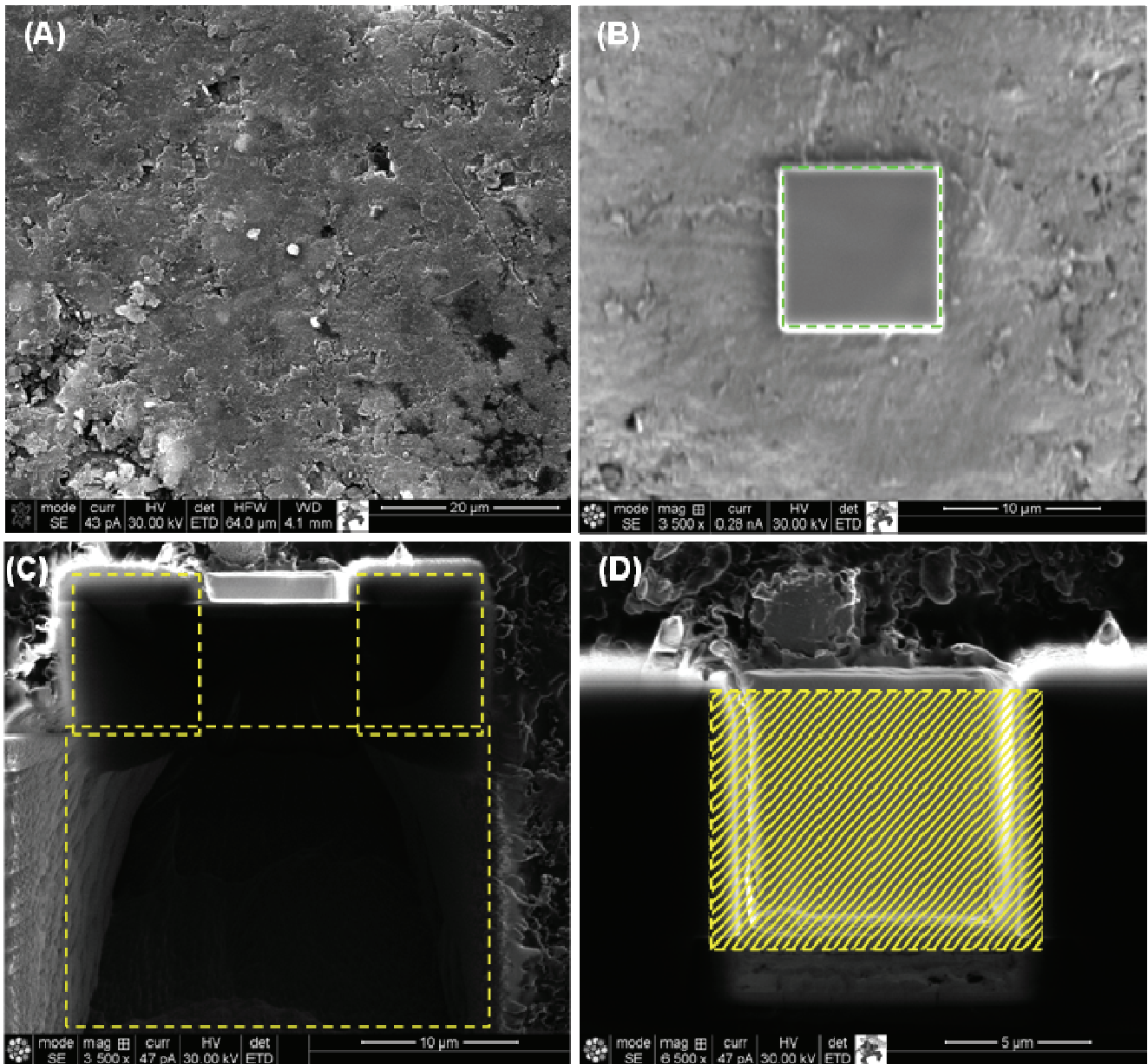
Fig. 5−SEM-FIB images of serial sectioning procedure: (A) Flat surface of the polished sample is allocated, (B) A 10×10×1.5 μm layer of platinum is deposited on the target area (~18 min), (C) Swimming pool is milled and cleaned (2−3 hrs), and (D) Automated slicing of a 10×0.05×25 μm area is performed and 200 slices are imaged sequentially (19−20 hrs).

Fig. 6 shows examples of micron- and nano pores of Utica shale after the swimming pool has been milled and cleaned. Shale gas has a complex pore structure that cannot be addressed by conventional core analysis. Intergranular pore sizes range from 15 to 50 nm. Another type of porosity, classified as interparticular or mineral porosity, occurs within the clay minerals. Its pore opening throat is about 5 nm.
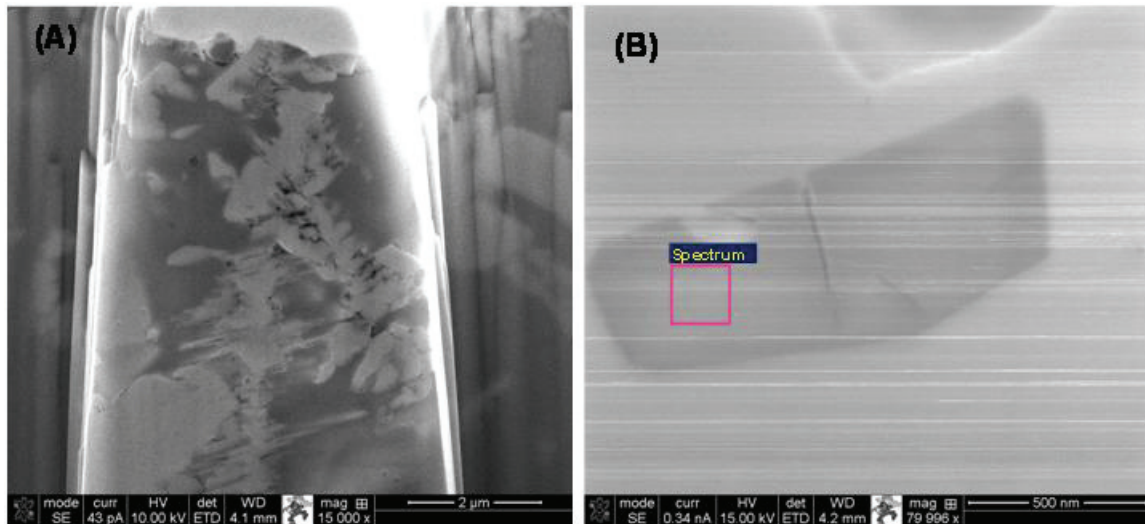
Fig. 6−Subsurface SEM image of Utica shale, Dolgeville Fm., at a depth of 4,878 ft; (A) Cross-section shows pores of less than 50 nm in diameter within the quartz grains, and (B) Close-up image clearly shows interparticular porosity.

As shown in **Fig. 7**, element analysis using EDS can analyze the captured spectrum of the grain in **Fig. 6B**. The black phase in the middle of the SEM image suggests the existence of pyrite mineral, because it results in a darker color phase, which indicates a higher atomic number and element spectrum confirms the presence of both iron and sulfur. However, since there is no clear relationship between atomic number and phase brightness for the secondary electron image, this dark phase was most likely caused by faster milling rate during the milling process. They were in slight recess compared with the bright phase. Although the silicon spectrum is high and quartz is very common in shales, it is probably from the result of deep x-ray beam penetration. Calcite may be present because natural fractures, which are healed by calcite, have been observed in Utica shale samples. The streaks in **Fig. 6B** are due to charging; and the atomic percentage in the spectrum is standardless. Gallium results from the ion beam source and should be disregarded.
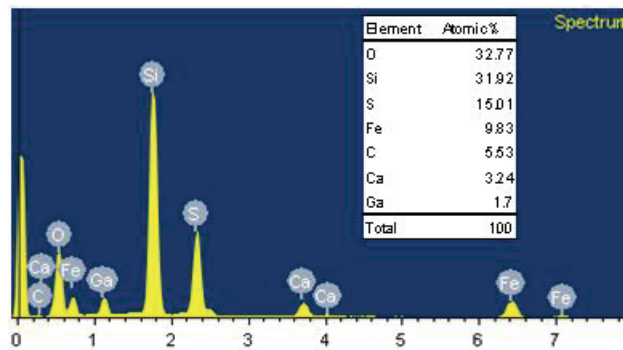

Fig. 7−EDS analysis of clay mineral present in Utica Shale sample, Dolgeville Fm., at a depth of 4,878 ft.

The SEM images of Utica shale in **Fig. 8** show clay platelets within the quartz grains which create inextricable structure with a variety of pore sizes. Diagenesis in shale gas rocks creates a complex mineral structure. Image 8(B) was captured on a freshly fractured surface. It represents shale organic matter (i.e. kerogen) and suggests a complex pore structure. It provides plenty of spaces to store adsorbed gas. Moreover, elemental composition analysis affirms the presence of carbon matter. The pores are configured in three dimensions. To characterize such a pore structure, a serial sectioning process was performed and a three-dimensional pore model built.
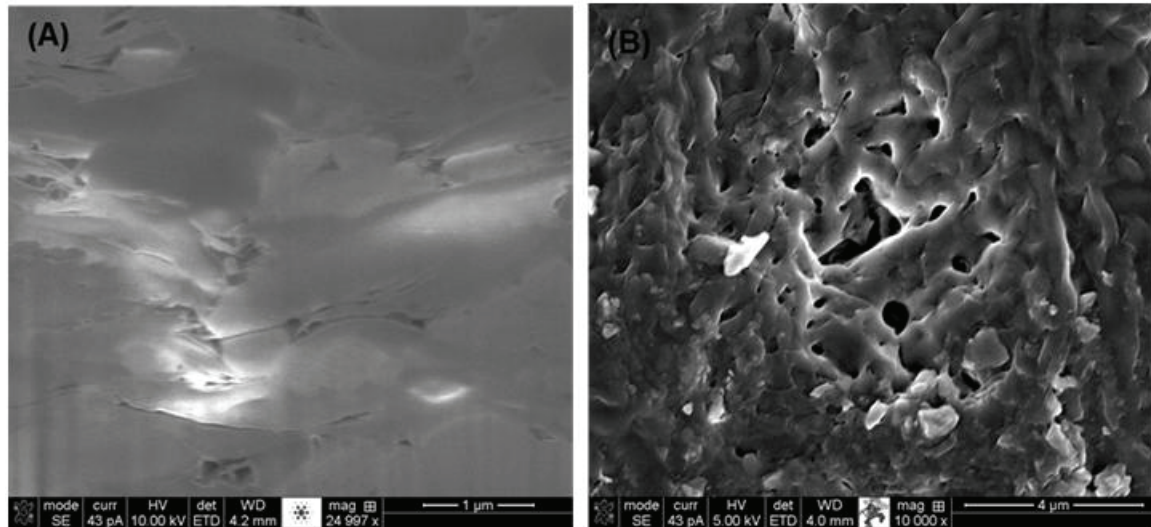
Fig. 8−SEM image of Utica shale, Indian Castle Fm., at a depth of 4,649 ft: (A) structural pores of various sizes apparent after milling, and (B) Large chunk of organic matter with a complex textile of pores.

Fig. 9 shows other features of Utica shale that were observed on a freshly fractured surface. Clay platelets are closely packed together and form a variety of micron and nano pores (< 2 μm), as shown in **Fig. 9(B)**. Pyrite framboids are shown in **Fig. 9(A and D)** micromorphological features that consist of pyrite crystals bound together. These structures provide a porous body. The pore sizes in this mineral are between 20 and 100 nm. Element analysis using the spectrum generated by the EDS detector confirms the existence of pyrites, in addition to other clay minerals, such as illlite, and nonclay minerals such as quartz and calcite as shown in **Fig. 10**. The section below on XRD results offers a more detailed clay and nonclay mineralogy. **Fig. 9(C)** is a BSE backscattered that clearly reduced the bright spots caused by high electron beam current charges on the target surface.
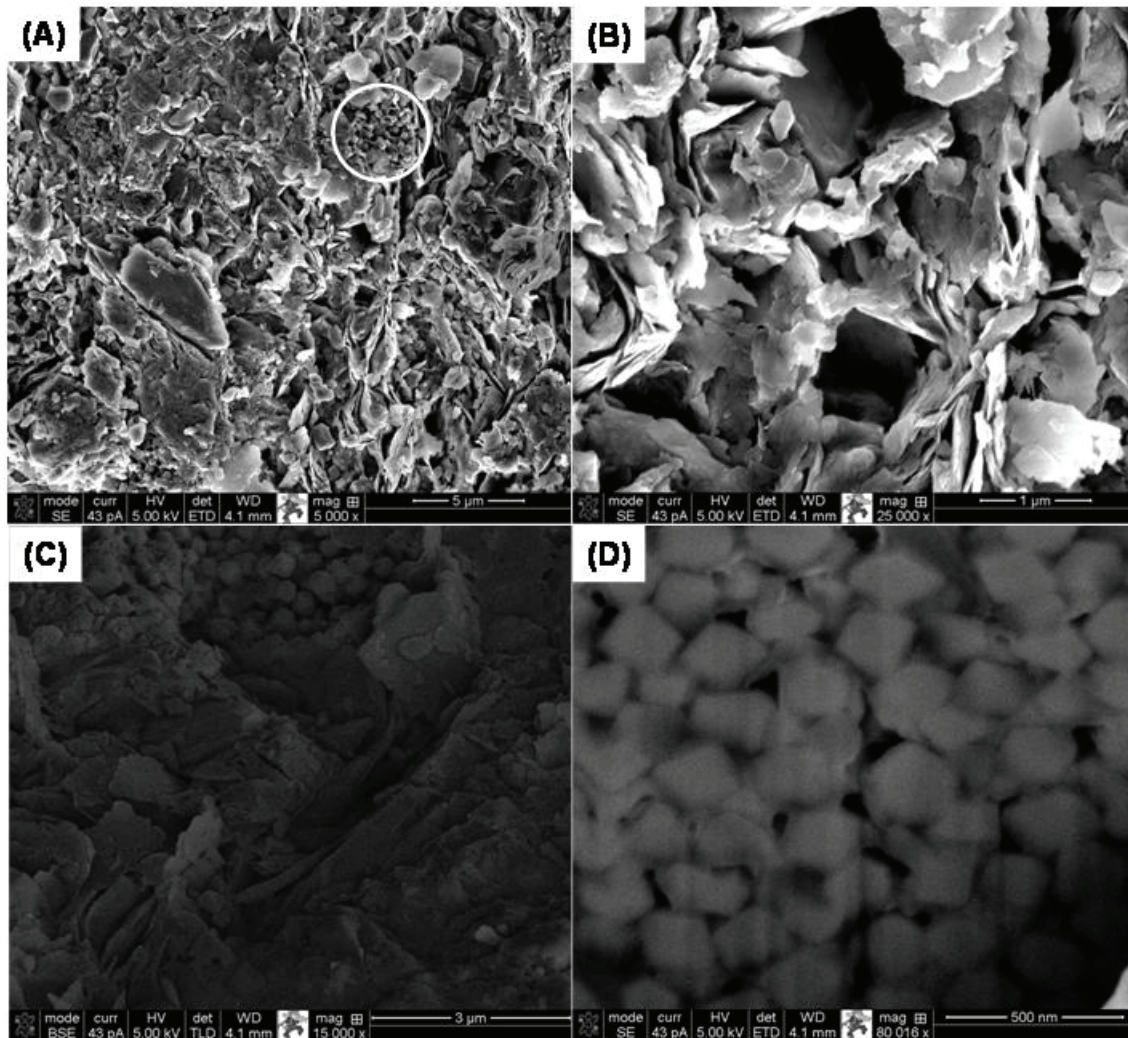
Fig. 9−SE/BSE images of Utica shale, Indian Castle Fm. at depth of 4,649 ft; (A) Fresh surface shows clearly different clay structure of pyrite framboids and clay platelet, (B) Zoomed-in micro- and nano-pores, (C) BSE image confirms pyrite framboids surrounded by clay platelet, and (D) Nano-porosity is observed within pyrite framboids.

Fig. 10 presents full spectrum map of Utica shale that suggests the existence of abundant minerals such as pyrite, illite, quartz and some calcite. Pyrite framboids are clearly seen where they are compositionally pyrite mineral (FeS_2) but they are roughly spherical aggregates of discrete equi-regular euhedral microcrystallites of around 0.25 µm in diameter, with the average aggregate size ranging from 5−20 µm. Illite is a very common clay mineral in gas shale source rock. It is compositionally class of aluminum silicates but structurally complex with wide range of properties. It is considered as non-swelling clay and has low cationic exchange capacity (CEC). Quartz is the second most abundant mineral in shale after clay minerals. Element mapping shows about 10% silicate exists in Utica shale. Calcite is a common mineral in the most Utica shale samples where it can be named as calcareous shale indicating high quantity of lime. XRD results section shows only Indian Castle sample from Utica shale exhibits less counts of calcite than samples acquired from Dolgeville formation.
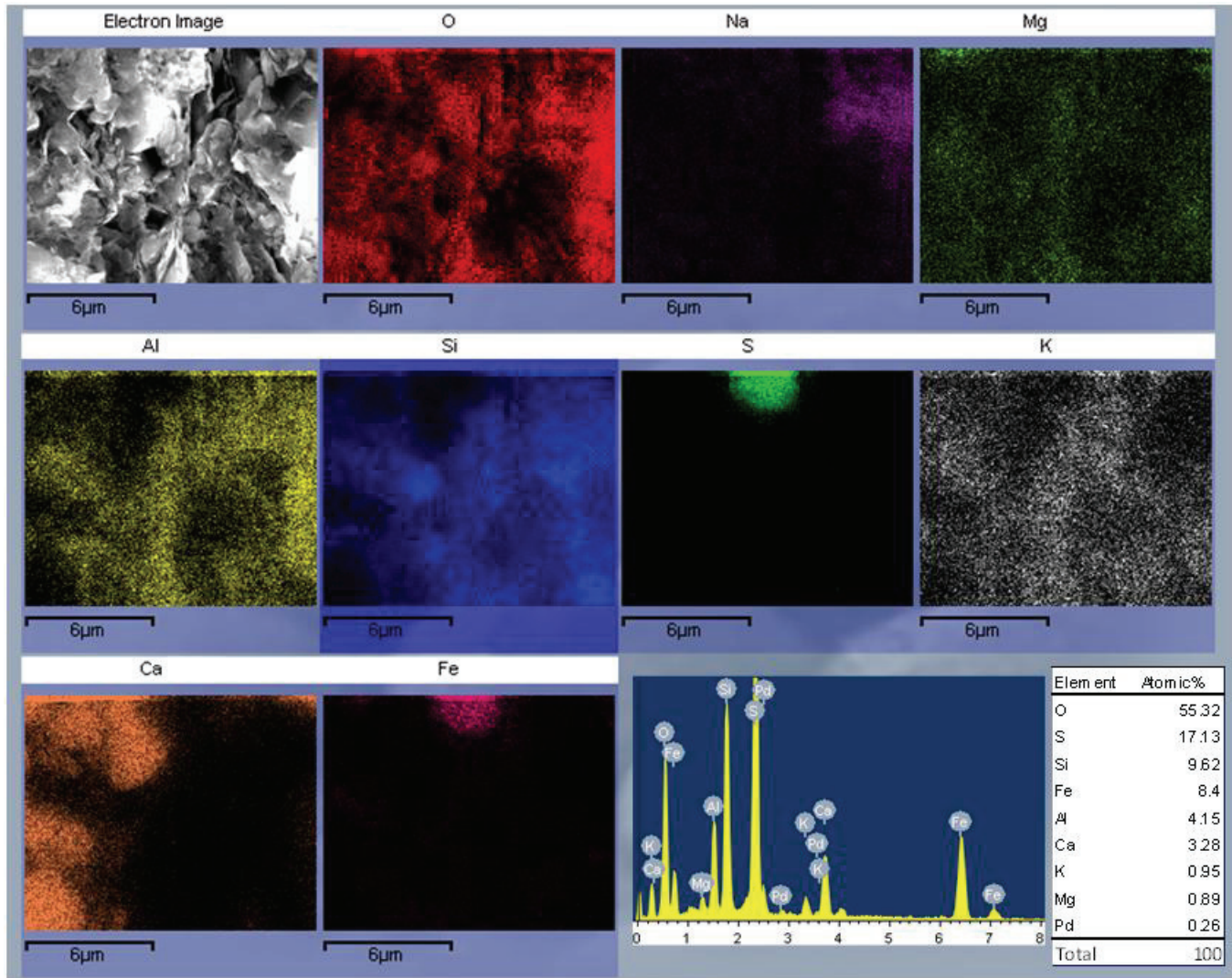
Fig. 10−EDS element mapping results of Utica shale, Indian Castle Fm. at depth of 4,649 ft.

Total organic carbon content (TOC) test has shown that Fayetteville shale sample contained the highest content compared to Utica and Haynesville shales. The reported TOC value was 4.04 wt. % by Elgmati et al. (2011). The same conclusion can be drawn from SEM images and element analysis results. **Fig. 11** illustrates three main features which can be seen on the SEM image of the milled surface of Fayetteville shale sample.

(1) A vuggy porosity which is marked in spot (A) with 2−8 μm pore size offers a sizable storing space for free gas.
(2) A porous kerogen is shown in image (B) which contains abundance of nano pores with size of 5−100 nm. To confirm kerogen entity, element analysis is performed and resulted in high carbon spectra between 37−42% as shown in **Fig. 12**.
(3) Many conductive natural fractures on image (C) shows opening size of 25−50 nm. The curtaining in this case is most likely due to the material itself and high ion beam milling voltage (30 kV).
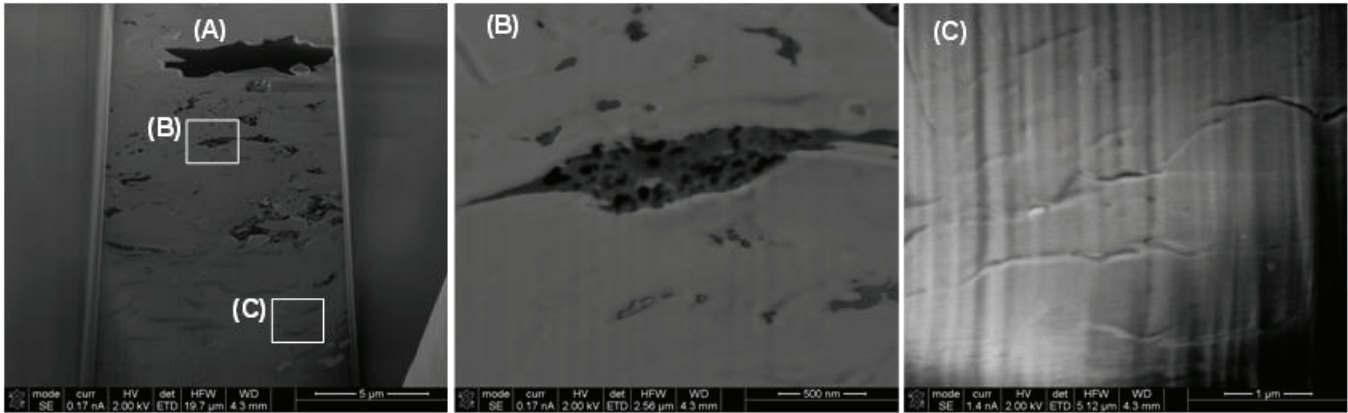
Fig. 11−SEM images of Fayetteville shale at depth of 2,351 ft; (A) Vuggy micro-porosity, (B) Kerogen nano-porosity occupies about 40−50% of the organic matter, and (C) Nano natural fractures.

Element anaylsis was performed at three positions as shown in **Fig. 12**. According to the spectrum counts, the dark porous spots represent kerogen matter which contains high carbon content. Meanwhile, the solid part is believed to represent aluminum silicate class mineral (possibly illite).
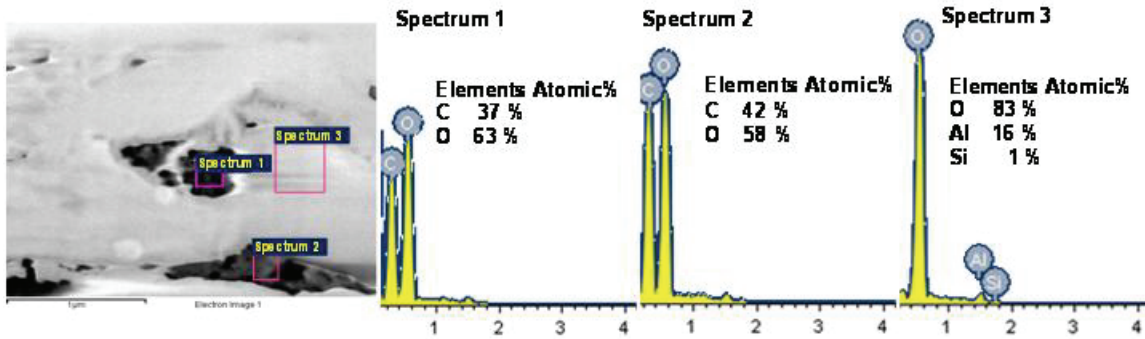

Fig. 12−EDS spectrum analysis of Fayetteville shale at depth of 2,351 ft, spectrum 1 and 2 confirm kerogen presence, and spectrum 3 represents aluminum silicate (clay).

3D Pore Model Reconstruction

After performing serial sectioning and sequential imaging of 200 images from the Fayetteville shale sample, all the two-dimensional SEM images were stacked into three-dimensional pore structural model. The process was performed into two main steps. The first step is achieved by creating a 2D SEM model of the kerogen nano pores as shown in **Fig. 13**. This was then translated into a 3D model. Commercial imaging softwares were used for reconstructing the three-dimensional model and obtaining and visualizing advanced qualitative and quantitative information from the shale gas SEM images. The original image (A) was converted into binary image (B) with pixel values of 0 and 1.
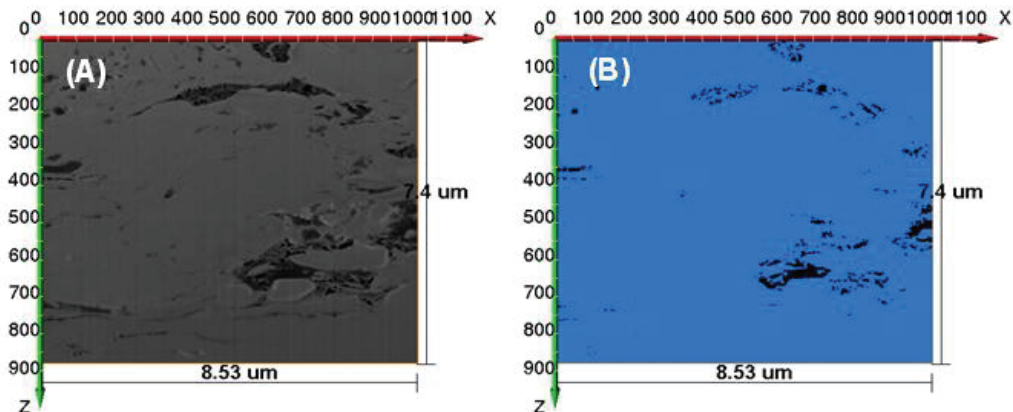

Fig. 13−Two-dimensional kerogen pore model of Fayetteville Shale at depth of 2,351 ft; (A) SEM images showing the organic matter, and (B) Converted 2D binary image of 0 and 1 pixel values.

A scale transformation from pixels into micrometers is done according to image size and magnification scale. A two-dimensional quantification module was utilized to handle the quantitative analysis of kerogen pore size calculation. However, this algorithm also works for micron-sized pores and fractures within the shale body. The resulted histogram of two-dimensional SEM model in **Fig. 14** presents micron-sized pores as the major pores. The extracted rock porosity is 3.34% and kerogen porosity occupies about 40−50% of organic matter. Kerogen nano pores are between 10−50 nm. The computed kerogen permeability is 4.76×10^{-4} md according to Kozeny equation by using average pore throat diameter of 30 nm. It is suggested to develop new technology which is capable to extract the adsorbed gas from the very tight pores through the macro hydraulic fractures. This definitely will maximize the unconventional gas reserve from shale gas plays.
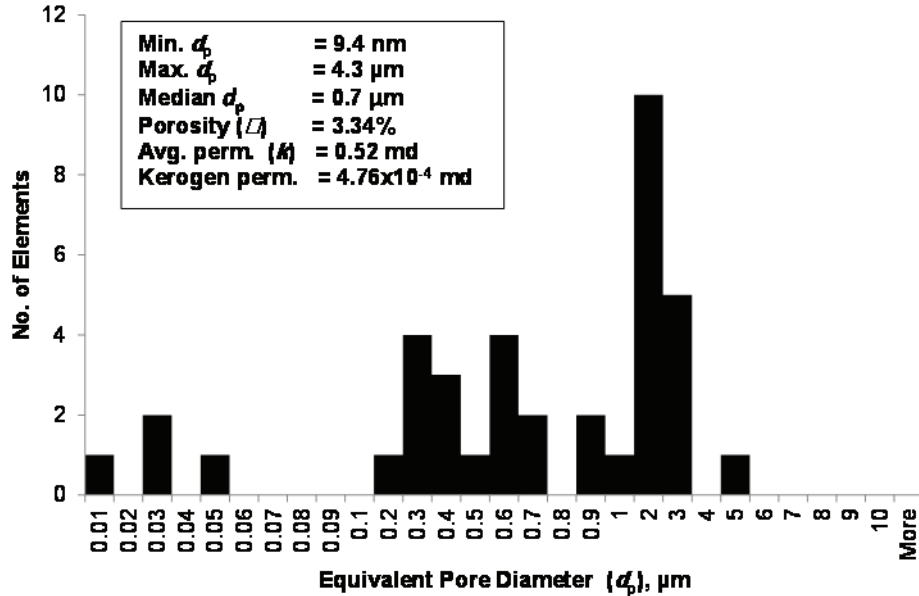

Fig. 14−Fayetteville shale kerogen pore size histogram resulted from two-dimensional pore model.

The second step, before stacking the images, involved the alignment process that was done at a marked feature on the image in order to eliminate the mechanical and beam drifts. Then, 200 slices were loaded into a three-dimensional bounding box. A representative elemental volume of $8.85\times8.65\times9.62$ µm was extracted from the bounding box. It is believed that the representative elemental volume is able to provide key insights into the petrophysical properties of the shale gas sample. Optional smoothing and filtration algorithms may be applied if required. Image voxels were converted into a meaningful scale (µm) by taking into account of the original image's magnification scale. Binary image conversion and separation were also required within the chosen voxel thresholds by using some quantification modules which are associated with the stacking software. It is used to determine grain element boundaries for defining the pore structure of shale gas. **Fig. 15** summarizes all these steps.
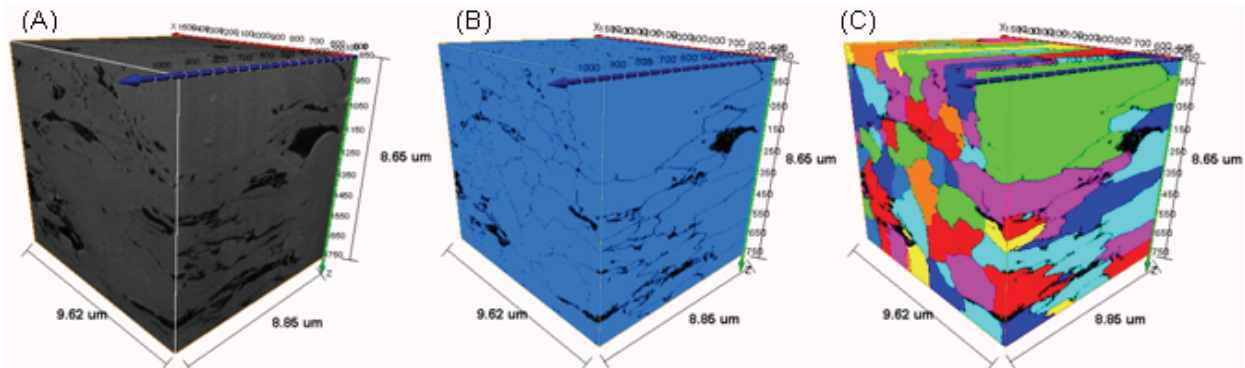

Fig. 15−Three-dimensinoal pore model of Fayetteville shale: (A) 200 slices of two-dimensional SEM images are aligned and stacked, (B) Converted three-dimensional stack to binary image of 0 and 1 voxel values, and (C) Element boundaries are determined and labeled to perform the porosimetry analysis.

Once all the previous steps are carried out, an analysis module is used to perform statistical analysis and to calculate rock pore size distribution according to the chosen separation algorithm. Moreover, total porosity, tortuosity and anisotropy were outputted. As seen from **Fig. 16**, the major pore size, which corresponds to the highest frequency, is 30 nm. This validates the

analysis of 2D kerogen model. Only a small number of micron-sized pores exist in this three-dimensional model. Rock permeability is determined by using the adjusted Kozeny equation which takes pores tortuosity into account as shown in **Eq. 2**.

Tortuosity coefficient ( ) is basically defined by the ratio of actual flow path (L_a) to the total sample length (L). It is always greater than 1 for heterogeneous rocks. From most rock laboratory standpoint, tortuosity can also be defined by the following equation.

Using anisotropy definition of vertical to horizontal permeabilities ratio (i.e. $\beta = k_v/k_h$) and assuming that horizontal permeabilities (k_x and k_y) in x and y directions are equal to k_h, both vertical and horizontal permeabilities were determined.
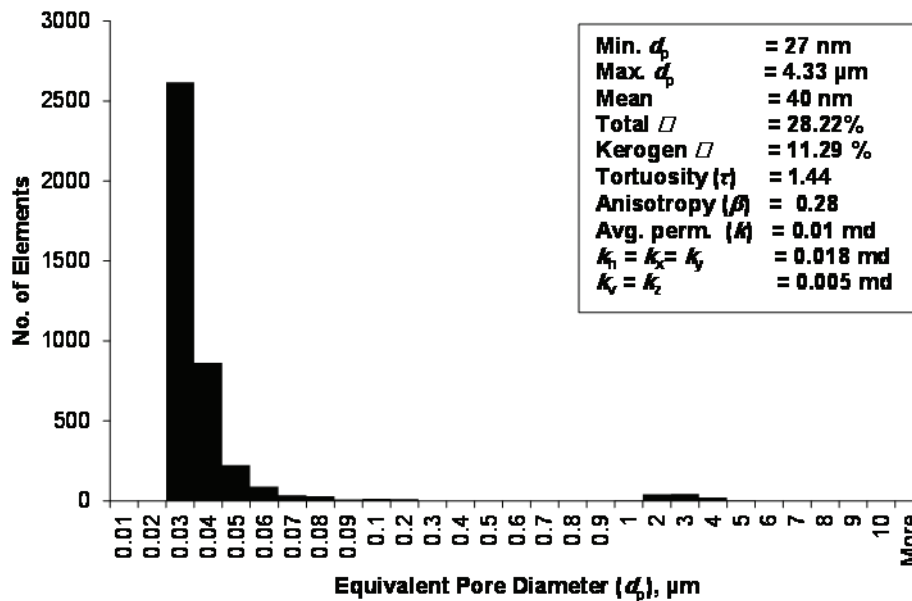

Fig. 16−Fayetteville shale pore size histogram resulted from 3D pore model.

In conclusion, submicron pore modeling is believed to be a powerful tool compared to MICP method. It provides direct measurement of the original pore structure and it also defines the bulk pores of the shale sample without any manipulation. Yet, the diagnosis scale is in submicron scale compared to the gigantic scale of the mercury porosimetry test. In order to make results universal, a comprehensive statistical study is required.

X-Ray Diffraction and Clay Mineralogy

As known that clay minerals are very fine grained that X-ray methods, rather than hand specimen or optical methods, are used to identify them. Moreover, clay structure is three dimensional and varies considerably from one type of clay to another. X-Ray diffraction is considered to be the best method in defining clay minerals. The qualitative identification procedure begins with searching for a mineral that has the strongest peaks, and follows with confirming the choice by finding the positions of weaker peaks for the same mineral. The most important relation for the use of X-ray diffraction is shown in Bragg's law, 1912.

where n is an integer (i.e. 1, 2, 3…, etc.), λ is the wavelength of the incident X-ray beam (1.54 Å for Copper), d is the distance between atomic layers in a crystal, and θ is the angle between the incident ray and the scattering planes. The diffraction planes are 00l= (001), (002), (003), (004).

By using basal spacings (d) and 2-theta for Cu K-alpha radiation in **Table 1**, clay and non-clay minerals peaks can be readily distinguished. Some mineral peaks may be invariant because the mineral structure tolerates no significant atomic substitutions. Our focus is at small diffraction angles, because most of the important clay peaks occur at 2-theta values of 40° or less; therefore, theta is 20° or less, and that value is sufficiently small to fit the foregoing argument to a pretty good approximation.

Table−1 Basal Spacings (*d*) in Å and 2θ for Cu K-Alpha Radiation*

Clay Mineral Group	001		002		003		004	
	Å	2θ	Å	2θ	Å	2θ	Å	2θ
Chlorite	14.1-14.2	6.2-6.3	7.05-7.1	12.5-12.6	4.7	18.9	3.52-3.54	25.3-25.1
Kaolinite	7.16	12.4	3.57	24.9	2.38	37.8	1.78	51.3
Mica (Illite)	9.97-9.98	8.8	4.96	17.9	3.32	26.8	2.49	36.1
Ca Smectite**	15.4-	5.7	7.7	11.5	5.1	17.4	3.8	23.4
Na Smectite	12.4	7.1	6.2	14.3	4.1	21.7	3.1	28.8
Ca Smectite - glycol	17-	5.2	8.5	10.4	5.7	15.6	4.2	21.2
Na Smectite - glycol	16.7							
Vermiculite	14.1-14.3	6.3		w		w		w
Non-Clay Minerals								
Calcite		29.5						
Dolomite		30.9						
Quartz		20.8		26.6				
Albite and Microcline		27.7						
Pyrophyllite		9.6		19.3		29.1		

* Adopted from modified procedure described by George S. Austin-New Mexico Bureau of Miners & Mineral Resources.
** General position of broad peaks.
w = weak if present at all.

Clay minerals are compositionally a class of aluminum silicates, and structurally they are complex with a wide range of properties. The basic building blocks are silica tetrahedral and aluminum octahedral. Carbonate minerals are commonly associated with clay minerals specially calcite and dolomite. Peak positions will vary with the limited solid-solution series between calcite and dolomite.

Yaalon (1962) applied normative calculations on the chemical composition of 10,000 shales and arrived at the following average composition: 60% clay minerals-mostly illite, 20% quartz, 10% feldspar, 6% carbonates, 3% iron oxide, and 1% organic matter. This agrees with the presented XRD results.

The specimens were examined three times on XRD instrument in different circumstances. Sometimes it is difficult to distinguish between chlorite and kaolinite when only weak peaks are present at 12.5° and 25° 2θ. Such a sample could contain only chlorite, only kaolinite, or a mixture of the two. In this situation, the sample is treated chemically or heated and then reexamined. To eliminate the possibility of any interference between the peaks of different clay minerals, the following procedure is implemented. Initially, the samples were examined before applying any treatment and the resulted run was marked as "Untreated". Then the samples were put in glycolation vessel for 24 hours to widen clay mineral layers for better mineral identification resolution. This run was called "Glycolated" run. The last run was performed after heating the samples up to 375°C for 1 hour and it was named "Heated" run.

Table 2 presents a summary of the semi-quantitative analysis of XRD results. Semi-quantitative assessments make the identification of individual minerals in shale gas samples much more valuable. Unfortunately, the intensity of a mineral's diffraction peaks cannot be directly used as an accurate measure of mineral abundance, because different minerals, different atomic planes within a mineral, and different samples of the same mineral do not have the same ability to diffract X-rays (Biscaye, 1965). However, this study uses the modified procedure for semi-quantification of clay minerals with approximate accuracy of ±10%. The computed clay mineral contents were often avoided because of their weak or doubtful peak intensity.

Table−2 Summary of Qualitative XRD Results

Shale Gas Source Rock Samples		Haynesville Shale 12,000 ft	Utica Shale Indian Castle Fm. 4,649 ft	Utica Shale Dolgeville Fm. 4,878 ft	Utica Shale Dolgeville Fm. 5,197 ft	Fayetteville Shale 2,351 ft
Clay minerals	Chlorite	31%	Low	-	-	-
	Illite	69%	High	V. Low	V. Low	Low
Non-Clay minerals	Calcite	Low	Low	High	High	V. Low
	Dolomite	-	V. Low	-	V. Low	V. Low
	Quartz	Moderate	Moderate	V. Low	V. Low	High
	Albite and Microcline	-	Low	-	-	-

Fig. 17 presents a combined plot of XRD results for five shale gas samples. Utica shale sample obtained from Indian Castle formation and Haynesville shale exhibit the highest amount of illite whereas the first strongest peak at 8.8° 2θ is obviously seen. Both of the Utica shale samples acquired from Dolgeville formation are classified as calcareous shale. XRD results also suggest high calcite content. Fayetteville shale may compositionally comprise of higher quartz content than illite because illite's peaks intensity is almost vanished.
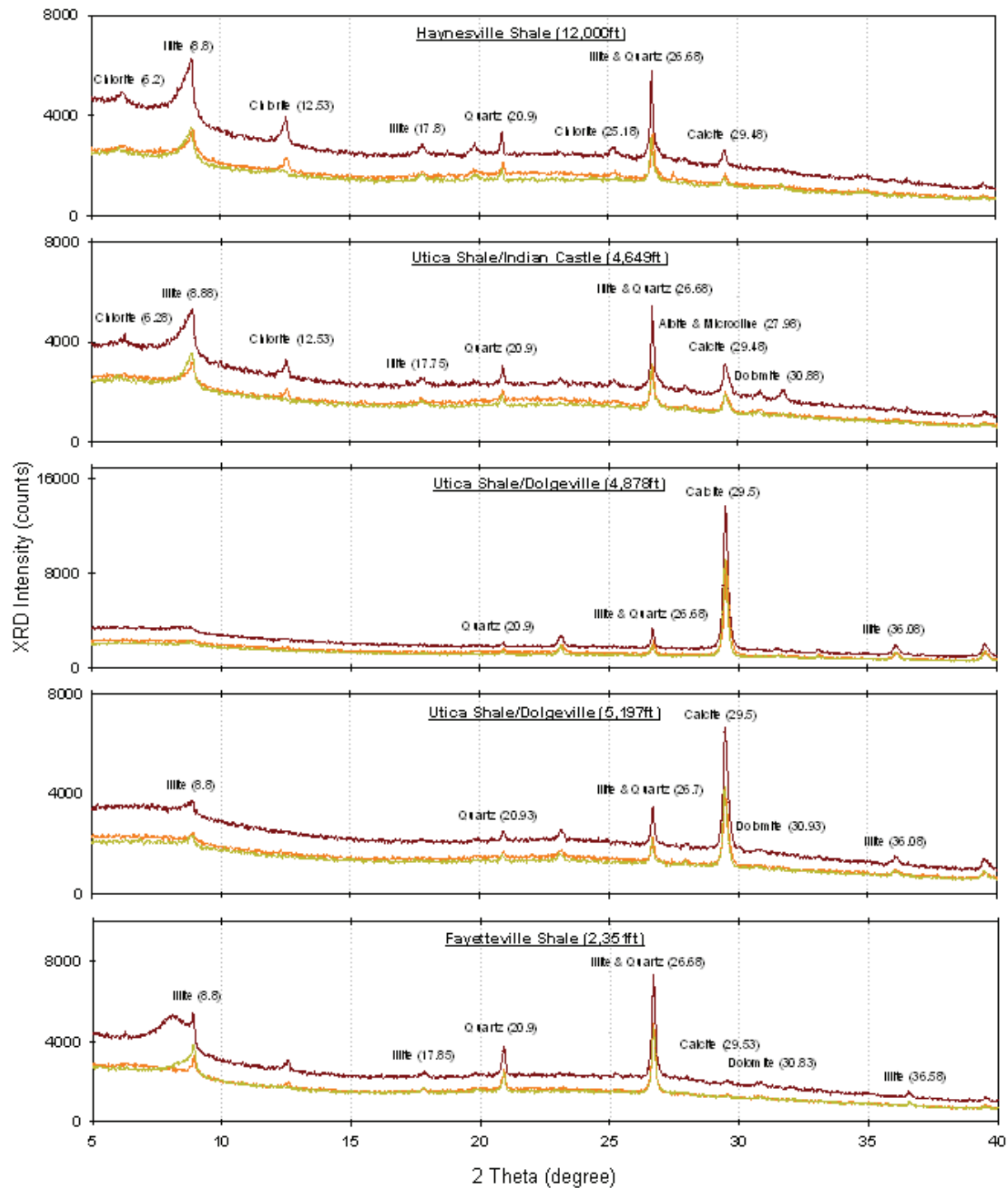
Fig. 17−X-ray diffraction results of the five shale gas samples.

Contact Angle Measurements

Shale gas rocks are usually hydraulically fractured in order to be capable to produce gas. Chemical additives such as friction reducers and viscosifiers have often been added into fracturing fluids. However, the additives in fracturing fluids may impair the fracture permeability and alter the rock wettability which influences the gas flow ability. To remedy this problem, intensive study of rock surface and fluid composition interaction should be performed in order to mimic the gas flow in submicron pores. Gas flow behavior in submicron pores of shale gas is controlled by rock mineralogy, organic matter content and fluid type. Clay minerals are very special and they are different than other minerals. All minerals are electrically neutral except clay minerals, which always negatively charged. They are the only minerals that are capable to exchange cation along the negative surface charges (ions). Therefore, clay minerals have high cation exchange capacity (CEC).

Rock wettability is basically defined by the contact angle measure. When only one fluid exists in the pore space, there is only one set of forces to consider, which is the attraction between the rock and the fluid. When more than one fluid phase is present, there are at least three sets of active forces affecting capillary pressure and wettability. The resulted contact angle from goniometer device which uses sessile drop technique is defined by the following equation:

$$\theta = 2 \, tan^{-1} \frac{2h}{d} \qquad (5)$$

where θ is the contact angle, h is the drop height and d is the drop diameter or width.

Polished plates of shale gas samples were used as representative surfaces for sessile drop and contact angle measurements. In our measurements, the specimen do not account for surface roughness, the material heterogeneity and the presence of organic matter. Alternative wettability measurement methods which are referred by Tiab and Donaldson, 1991 could be one of the best tools for shale gas wettability study.

Fig. 18 presents the results of contact angle measurements onto the five shale samples using six chemical additives of fracturing fluid. All contact angle results were compared to deionized water (DIW) contact angle and summarized in **Table 3**. The six additives are comprised from two polymers (e.g. FRW-18 and FRW-20) and four surfactants (e.g. Inflo-45LB, Inflo-250, GasFlo-G, and Flowback-30). The examined solutions were made of 0.1% wt. concentration. The presented results were repeated at least three times for each shale chip.

Table−3 Contact Angle Results Summary*

Shale Gas Source Rock Samples	Haynesville Shale 12,000 ft	Utica Shale Indian Castle Fm. 4,649 ft	Utica Shale Dolgeville Fm. 4,878 ft	Utica Shale Dolgeville Fm. 5,197 ft	Fayetteville Shale 2,351 ft
DIW	14.0	42.5	81.8	64.6	47.8
0.1% FRW-18	23.8	28.2	73.4	36.5	21.8
0.1% FRW-20	20.4	23.1	38.3	29.6	16.5
0.1% Inflo-45LB	0.0	0.0	13.0	0.0	0.0
0.1% Inflo-250	0.0	0.0	28.2	0.0	0.0
0.1% GasFlo-G	0.0	0.0	41.6	0.0	0.0
0.1% Flowback-30	24.7	14.1	36.8	21.2	15.3

* Contact angle results have accuracy of ± 5 deg.

It is highly observed that all the tested fracturing fluid additives on Utica and Fayetteville shale rock samples result in reducing the contact angle and making the shale rocks behave more water-wet like surface compared to DIW contact angles. The scenario for Haynesville shale sample is slightly different, whereas both polymers and Flowback-30 surfactant tend to slightly raise the contact angle to intermediate water-wet level. This might be attributed to 1) very high illite concentration (70%) as illite peak intensity on XRD data suggests and 2) low organic matter content of Haynesville shale (TOC = 0.81 wt. %) as reported by Elgmati et al. (2011).

Utica shale samples acquired from Dolgeville formation result in the highest DIW contact angle which is between 60−80°. This rock behaves like oil-wet material. X-ray diffraction results suggest high concentration of calcium carbonate (calcite). However, Utica shale sample acquired from Dolgeville formation at depth 4,878 ft behaves slightly different when it is treated with all surfactants and polymer FRW-20. These solutions have high tendency of altering wettability of this rock to water-wet with contact angle of 10−30°. Polymer FRW-18 impairs this surface wettability toward water-wet very slightly. This is attributed to fracturing fluid chemical composition and clay mineralogy. It is noted that this sample is classified as calcareous shale sample and sometimes it is also called carbonate-like shale. This rock sample is very hard to saw. It is likely attributed to 1) very high lime content as calcite peak intensity in XRD results suggests and 2) extremely low organic matter content (TOC = 0.31 wt. %) as documented by Elgmati et al. (2011).

In the most presented cases, surfactant solutions alter shale wettability to strongly water-wet system except surfactant Flowback-30 which behaves like polymers. Both polymer solutions alter the wettability of shale gas rocks in the same manner with resulted contact angle of 20−30° except Utica shale sample acquired from Dolgeville formation at depth of 4,879 ft. For this shale sample, only polymer FRW-18 results in high contact angle of 62°.

To sum up, shale gas wettability changes to oil-wet when high concentration of calcite exists. Organic matter content governs fracturing fluid wettability alteration. Low organic matter content would have tendency to change wettability of calcareous samples to oil-wet system. Wettability of shale gas samples was demonstrated to have the tendency of changing to oil-wet when high concentration of calcite existed.
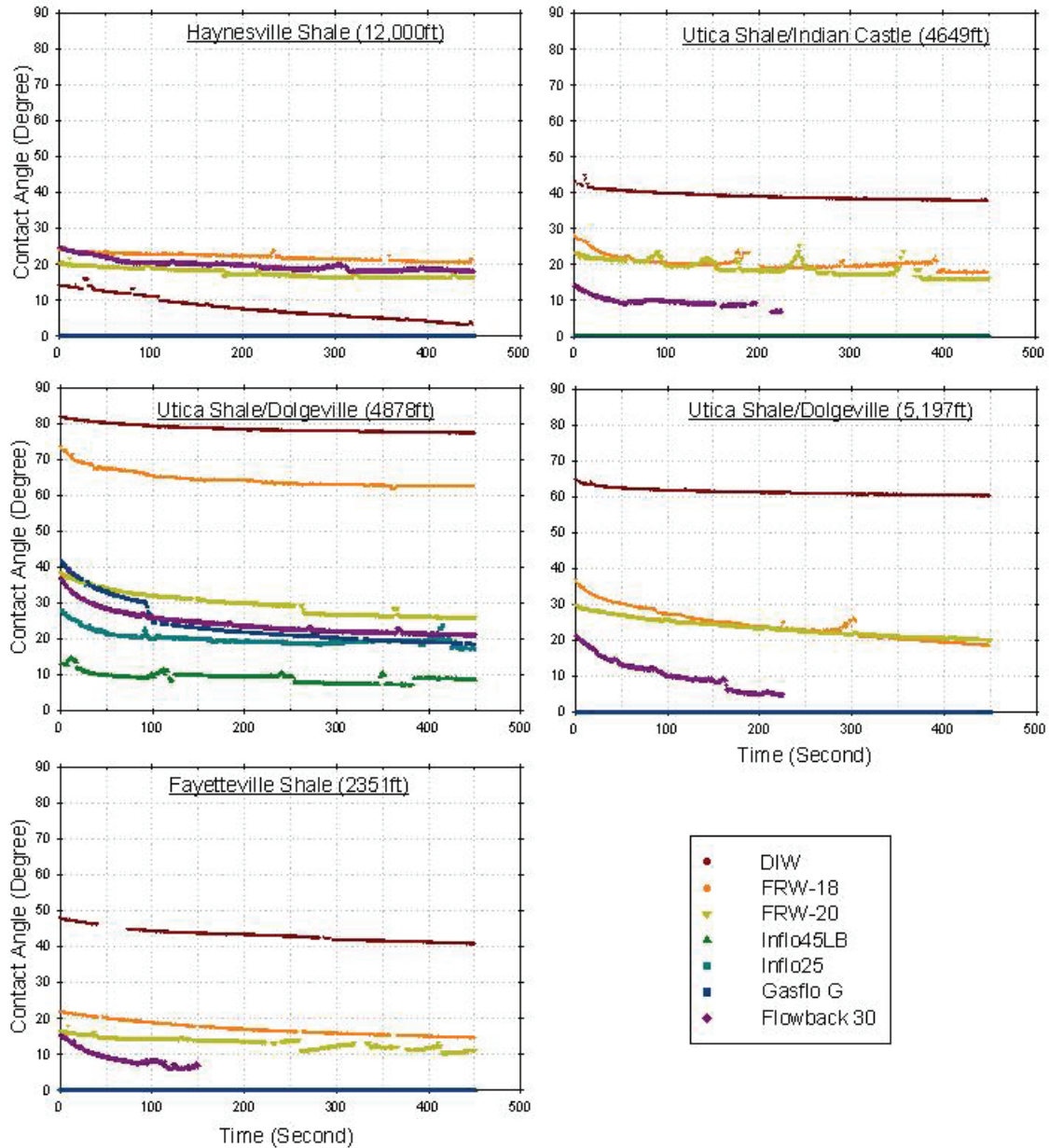
Fig. 18−Contact angle results of the five shale gas samples using six fracturing fluid additives.

Conclusions

This study supports the following conclusions:

1) Submicron pore networking and rock tightness greatly affect MICP results. The Haynesville shale sample exhibited extremely low matrix permeability with a pore size of 2−20 nm; however, fractures with large openings could dominate gas transportation. The Utica shale sample offered better matrix permeability, with a pore throat size of 20−200 nm.

2) A robust, detailed sequential milling and imaging procedure using SEM-FIB proved successful. SEM images showed many porous bodies that could be favorable candidates for gas storage. Various types of porosities (e.g., interparticular, intergranular, kerogen, vuggy, pyrite framboids, and fractures) were observed. Pores of organic matter were found in nano-sizes occupying 40−50% of the kerogen body.

3) The reconstructed three-dimensional pore model of Fayetteville shale gas sample provided numerous petrophysical properties such as pore size distribution, porosity, tortuosity and anisotropy.

4) XRD analysis provided insight into clay and nonclay mineralogy. It showed high illite content in the Haynesville and Utica shale samples. It also suggested high calcium carbonate (lime) content in the Utica shale samples.

5) Calcite content proved the dominant factor increasing the shale gas contact angle and changing the wettability of shale gas rock to oil-wet. Organic matter content governed the wettability alterations of calcareous samples.

Acknowledgments

References

Amyx, J.W., Bass, D.M., Jr., and Whiting, R.L. 1960. *Petroleum Reservoir Engineering: Physical Properties*. New York City: McGraw-Hill Book Co.

Biscaye, P.E. 1965. Mineralogy and Sedimentation of Recent Deep-sea Clay in the Atlantic Ocean and Adjacent Seas and Oceans. *Geological Society of America, Bulletin* **76**: 803-832.

Civan, F. 2000. *Reservoir Formation Damage: Fundamentals, Modeling, Assessment and Mitigation*. Houston, Texas: Gulf Publishing Co.

Elgmati, M., Zobaa, M., Zhang, H., Bai, B., and Oboh-Ikuenobe, F. 2011. Palynofacies Analysis and Submicron Pore Modeling of Shale-Gas Plays. Paper SPE 144267 presented at North American Unconventional Gas Conference and Exhibition, The Woodlands, TX, USA, 12-16 June.

Ghosh, S.K., Urschel, S.F., and Friedman, G.M. 1987. Substitution of Simulated Well-Cuttings for Core Plugs in the Petrophysical Analysis of Dolostones: Permain San Andres Formation, Texas. *Carbonates and Evaporites* **2**: 95-100.

Jones, N. 1996. *X-ray Mineralogy and the X-ray Diffractometer.* Oshkosh, Wisconsin: University of Wisconsin Oshkosh.

Kopaska-Merkel, D.C., and Amthor, J.E. 1988. Very High-Pressure Mercury Porosimetry as a Tool in Reservoir Characterization. *Carbonates and Evaporites* **3**: 53-63.

Leverett, M.C. 1941. Capillary Behavior in Porous Solids. *Trans. AIME* **142**: 152-169.

Liviu T., Dmitriy S., and Velimir R. 2007. Analysis of Chalk Petrophysical Properties By Means of Submicron-Scale Pore Imaging and Modeling. *SPEREE* **10**(3): 285-293. SPE-99558-PA.

Moore, D.M., and Reynolds, R.C. 1989. Jr. *X-Ray Diffraction and the Identification and Analysis of Clay Minerals*. New York City: Oxford University Press.

Sondergeld, C. H., Ambrose, R. J., Rai, C. S., and Moncrieff, J. 2010. Micro-Structural Studies of Gas Shales. Paper SPE 131771 presented at the Unconventional Gas Conference, Pittsburgh, PA, USA, 23-25 February.

Tiab, D., and Donaldson, E. 1996. *Petrophysics: Theory and Practice of Measuring Reservoir Rock and Fluid Transport Properties*. Houston, TX: Gulf Publishing Co.

Wardlaw, N.C., and Taylor, R.P. 1976. Mercury Capillary Pressure Curves and the Interpretation of Pore Structure and Capillary Behavior in Reservoir Rocks. *Bulletin of Canadian Petroleum Geology* **24**(2): 225-262.

Wyllie, M.R.J., and Gardner, G.H.F. 1958. The generalized Kozeny-Carman equation. *World Oil* **146**(4): 121-128.

Yaalon, D.H. 1962. Mineral Composition of Average Shale. *Clay Mineral Bulletin* **5**(27): 31-36.